Chapter 12
Low Energy Ion Beam Modification of Nanostructures

Christian Borschel and Carsten Ronning

Abstract Nanostructures and nanomaterials with their meso-scopic properties, which can be integrated into functional devices, will enable a variety of new applications in future. They can be grown with specific properties by plenty of physical and chemical methods, and subsequent modification using ion irradiation significantly expands the potpourri of functionality of this important material class. As the ion range becomes comparable to the size of the small structures, important effects must be considered in experimental planning: reduced incorporation of implanted species, morphological changes induced by point defects, as well as strongly enhanced dynamic annealing and sputtering.

12.1 Introduction

Nanotechnology is considered to be one of the future technologies, which will strongly influence our daily life in many different aspects. Already today, it affects many industrial areas: such as computing, pharmaceuticals, cosmetics, textile, sensing, or functional coatings. The major background is not only to make materials smaller and smaller in order to store or process more and more information. Of course, this is also a very important issue and well in line with Moore's law. However, the additional key point of the nanotechnology revolution within the next decades will be the capability to make use and advantage of meso-scopic properties of such nanosized materials. These properties can strongly differ from the respective bulk counterparts due to quantum confinement or the high surface-to-volume ratio enabling new functionality of nanomaterials. Such new functionalities will be discovered and developed in future for yet unknown applications opening new

C. Borschel · C. Ronning (✉)
Institut für Festkörperphysik, Friedrich-Schiller-Universität Jena, Max-Wien-Platz 1, 07743 Jena, Germany
e-mail: carsten.ronning@uni-jena.de

C. Borschel
e-mail: borschel@iradina.de; chrbor@gmx.de

W. Wesch and E. Wendler (eds.), *Ion Beam Modification of Solids*,
Springer Series in Surface Sciences 61,
DOI 10.1007/978-3-319-33561-2_12

horizons in a variety of areas. This paradigm has been aptly called “More than Moore”.

In order to meet the above described high expectations, nanotechnology relies on the reproducible and exact design of nanomaterials either by top-down or bottom-up synthesis approaches. Top-down techniques essentially use traditional workshop or microfabrication methods, where externally controlled tools are used to mill, cut, and shape materials into the desired size and shape. The most impressive product out of this route is for example a modern multicore processor with billions of transistors on a single chip. On the other hand, bottom-up synthesis methods make use of the self-assembly ability of small building blocks (such as atoms or molecules) forming automatically hierarchy and/or complex structures—here, the most impressive example is of course the human body formed just out of one DNA molecule. Both approaches have their advantages and disadvantages, and already today a huge potpourri of different synthesis techniques is available for both routes. Ion beam techniques are also among them and an important tool for nanomaterial synthesis as outlined already in some previous chapters of this book (Chaps. 4 and 11).

Even though a huge number of different nanomaterial systems can be realized with sophisticated synthesis methods, a lot of desired nanostructures are still and will remain also in future inaccessible due to chemical and physical reasons, because most synthesis methods work close or even at thermodynamic equilibrium. Issues like solubility limits or surface reconstructions are difficult or even impossible to overcome during synthesis. One alternative option is the subsequent modification of prepared nanomaterials using energetic ion beam irradiation, which enables processes far from thermodynamic equilibrium. This can result into metastable phases of the nanomaterials/nanostructures with unusual or even exotic structural, electrical, optical or magnetic properties, which is fully in line with the desired paradigm “More than Moore”. Furthermore, ion beam implantation is a very precise and controllable doping method and a well-known standard technique in industry. It was established already in the 70s, but until lately mainly used for the electrical doping of bulk or thin film semiconductor materials.

Whereas the structural changes of buried nanomaterials using high-energetic ion beams are described in Chap. 11, this chapter focuses on doping of exposed or free nanostructures (typically lying on a supporting substrate) using ion beams in order to precisely tune their electrical, optical, and magnetic properties. For such a goal, it is therefore necessary to adjust the ion range of the implanted species to the dimension of the nanostructures. As the material sizes are so small, typical low ion energies between 1 and 100 keV are used for doping and modifying nanostructures, and thus one can assume that nuclear stopping is the major involved process while electronic stopping plays a minor role (see Chap. 1).

We will see that the subsequent dissipation of the total deposited energy (both introduced by nuclear and electronic stopping) into the confined nanostructure strongly affects the resulting structure and properties. In most cases this effect even “overwrites” the collision cascade. Furthermore, sputter yields as well as damage and implantation profiles are completely different for nanostructures compared to

the bulk or thin film situation, because of the existence of additional surfaces in lateral directions. All these effects will be described in this chapter in detail, and additionally a few examples will be presented for semiconductor nanowires and nanoparticles.

12.2 Simulations

Monte Carlo (MC) simulations are frequently used to determine the distribution of ions implanted into the target and the distribution of ion beam induced defects created in the target (vacancies, interstitials). These MC simulation codes calculate collision cascades by simulating binary collisions with a random distribution of impact parameters, see details in Chap. 1. One of the most used MC codes is TRIM (Transport and Range of Ions in Matter) [1]. There exist several variants and derivates of TRIM for special applications. Examples are `TRIM.SP` [2] for sputtering calculations, or TRIDYN [3] for calculations with dynamic variation of the target composition.

In these MC simulation codes, the structure and morphology of the target must be represented and defined. In "conventional" MC codes based on TRIM the target is defined by a stack of layers, which are flat and which usually have infinite/periodic lateral extension. This way of defining the target limits the applicability of these MC codes to the ion irradiation of bulk targets or layered targets with a flat surface and flat interfaces. Nanostructures cannot be represented in these simulation codes, which is especially a problem for *free-standing* nanostructures. Nevertheless, these bulk simulations are sometimes used when irradiating nanostructures. The simplest way of adapting bulk simulations to nanostructured targets would be to take the distribution of implanted ions or the distribution of damage from bulk simulations and "cut out" the shape of the nanostructures; however, this method does certainly not yield accurate results. A more advanced method would be to take collision cascades simulated in bulk, and apply these cascades to the nanostructure while adjusting the correct point of entry where the ions hit the nanostructure surface. This is schematically illustrated in Fig. 12.1a, b. Nevertheless, this method will also yield inaccurate distributions of implanted ions and damage, as illustrated in Fig. 12.1c: The surface of the nanoparticles cuts right through the collision cascade, but the influence of the surface *on* the collision cascade is neglected, because the cascade was simulated for bulk. Errors are caused by ions/recoils, which move out of the particle and re-enter it, as well as the neglected influence of the surface binding energy E_s at the nanoparticle surface. Consequently, the correct three-dimensional (3D) structure and surface of the target must be represented in the program already during the simulation in order to obtain accurate distributions of implanted ions and damage. This is especially true, when the size of the nanostructure is in the same range as the size of the collision cascade.

Different approaches are used to simulate the ion irradiation of nanostructures, depending on the application and the desired accuracy (see Fig. 12.2). For very

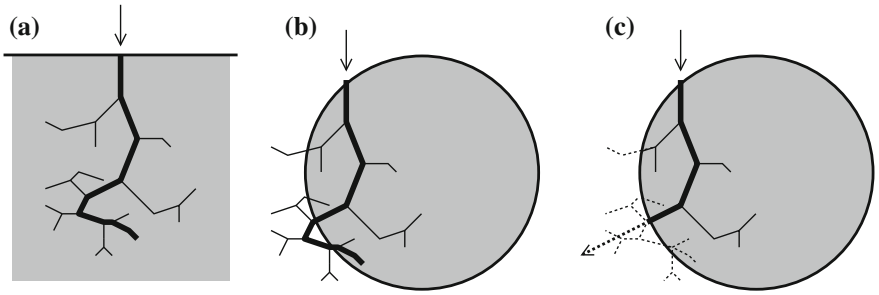

Fig. 12.1 **a** Collision cascade simulated in bulk material. *Bold line* path of the ion, *thin lines* recoils. **b** Applying the same collision cascade to a spherical nanoparticle. The cascade protrudes out of the particle. **c** In reality, parts of the cascade (*dashed lines*) would not exist in the nanoparticle

small nanostructures, full molecular dynamic (MD) simulations can be performed, as discussed in the Chap. 11. These MD simulations can inherently be much more accurate than MC simulations, because they avoid approximations like binary collisions and they can correctly simulate target temperatures above 0 K. However, the MD simulations require many orders more of computation time than MC simulations, because the equation of motion must be solved for every single target atom including all the interacting forces. Thus, MD simulations today are only feasable for small target structures of up to few tens of nanometers and only a small number of ions (a few hundred) can be simulated [4, 5].

A completely different approach is used to simulate the ion irradiation within a Focused Ion Beam (FIB) system. Here, one wants to know, how a surface or a nanostructure evolves under irradiation with a finely focused intense low-energy ion beam. There are simulation codes that calculate the evolution of the surface topography by taking into account sputtering and redeposition of sputtered atoms, (for example AMADEUS [6, 7]), see Fig. 12.2b. However, these codes are usually specialized to calculate sputter yields and related phenomena but do not perform the calculation of a collision cascade *within* the material and hence cannot be used to obtain the distribution of implanted ions or damage within nanostructures.

The third approach to simulate ion irradiation of nanostructures is using Monte Carlo simulations similar to TRIM but with a flexible 3D representation of the target (Fig. 12.2c). A versatile way to represent the target structure in the code is using a 3D rectangular grid with small rectangular cells instead of using a stack of layers, as illustrated in Fig. 12.3. Each cell can be filled with a certain material. Free standing nanostructures can be represented by setting the surrounding cells to vacuum. Furthermore, it is possible to make use of periodic boundary conditions for periodic arrays of nanostructures in order to keep the simulation volume as small as possible. The number of cells required in 3D simulations is typically much larger than the number of layers in a “conventional” MC simulation, resulting in much greater demand for memory during simulation. Furthermore, a larger number of ions has to be simulated to obtain good statistics for all cells, and additionally, for

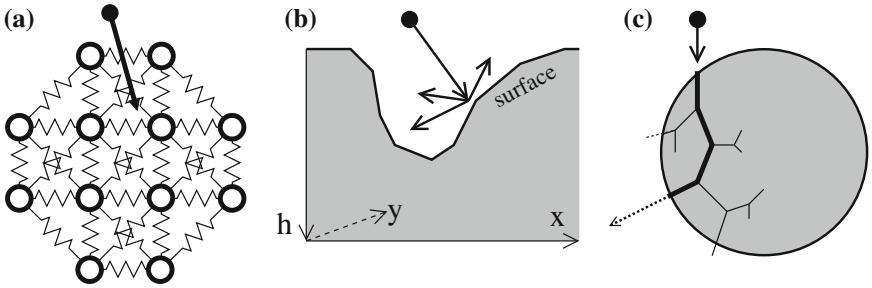

Fig. 12.2 Three approaches to simulate ion irradiation of nanostructures: **a** MD codes take into account all atoms in the target, their interaction potentials and solve the equation of motion numerically. **b** Surface evolution codes represent the target as a surface $h(x, y)$ and calculate the surface evolution due to sputtering and redeposition. **c** MC codes follow the projectiles and recoils from collision to collision

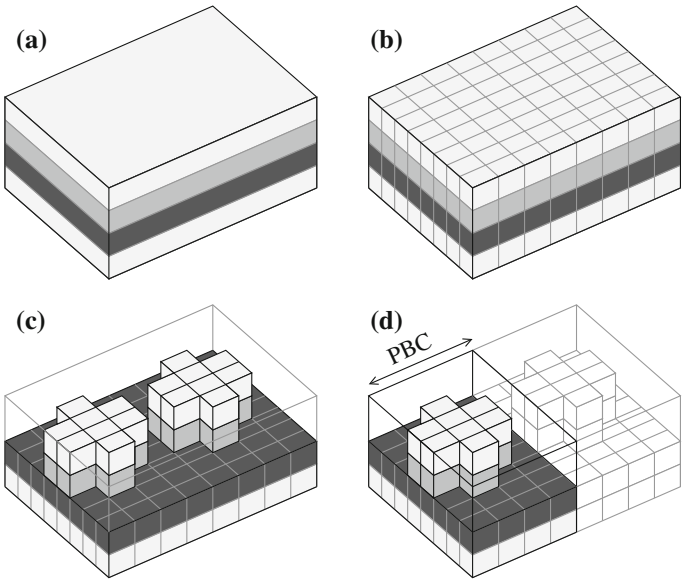

Fig. 12.3 **a** Conventional MC codes use flat, layered targets. Each layer consists of one material. **b** Division of target into rectangular cells. **c** Setting certain cells to vacuum allows representing free-standing nanostructures. **d** Periodic Boundary Conditions (PBC) can be used in order to reduce the simulation volume for periodic structures or samples with translational symmetry

small nanostructures it not possible to use large free path lengths as can be used in TRIM. In contrast, the free path lengths should be smaller than the cell size. Due to these additional requirements in computing resources, the 3D MC codes need to be optimized and often use special techniques in order to save computing resources. Examples are codes, which are used to simulate ion implantation in laterally

structured semiconductor devices, like for instance MCIMPL [8] and TOMCAT [9]. Techniques like trajectory replication, spatial octree division [9, 10], or convolution of point response functions [11] are used to save computation time. Another possibility is to speed up the simulations by avoiding the computation of transcendental functions during the simulation of the binary collisions. This can be achieved by using tabulated values for the scattering angle θ as a function of reduced energy ε and reduced impact parameter b for each combination of projectile and target nucleus Z_1 and Z_2, and combining this with clever indexing mechanisms to access the tables. This technique was first suggested by Yuan et al. [12] and later improved by Schiettekatte [13]. It is employed in the freely available 3D Monte Carlo simulation code *iradina* (**i**on **r**ange **a**nd **d**amage **i**n **na**nostructures) [14, 15], which is explained in the following and used for the simulations throughout this chapter.

Iradina uses a rectangular grid with rectangular cells to describe the target structure (as illustrated in Fig. 12.3). A list of materials can be defined in the program and one of the materials is assigned to each cell, or alternatively vacuum. The transport of ions and recoils is calculated similarly to TRIM, except that only small path lengths in the range of the average atomic distance are used and that the scattering angles in each collision are looked up from tables instead of using the MAGIC algorithm employed in TRIM, making *iradina* much faster. Whenever a projectile (ion or recoil) moves from material into vacuum or vice versa, the surface binding energy E_s is taken into account in order to calculate sputter yields appropriately. *Iradina* is intended for low energy ion irradiation where nuclear energy loss dominates, but the electronic energy loss is also taken into account using tables from SRIM [1]. *Iradina* is non-interactive and can perform simulations for other programs in the background, but a graphical user interface is available, which allows a simple object based definition of the target structure and easy use of the program.

The ion irradiation of perpendicular nanowires will be discussed in the following as an example for the usage of *iradina* and to show, why it is indeed necessary to take into account the correct 3D geometry of the target during the simulation of ion irradiation. Suppose a long cylindrical nanowire (NW) standing perpendicular on the substrate shall be irradiated from the side, as illustrated in Fig. 12.4a. It is not necessary for the simulation to represent the complete NW; instead we can take a small segment of the NW and apply periodic boundary conditions (PBC) along the nanowire axis. This leads to a nanowire of infinite length, which is a very well acceptable approximation for a long and thin nanowire. The simulation volume is always rectangular in *iradina* and is placed around the NW as illustrated in Fig. 12.4b. The simulation volume is divided into appropriate small rectangular cells; the cells inside the NW are filled with its materials, the cells outside the NW are set to vacuum, as illustrated schematically in Fig. 12.4c. The irradiation with ions is simulated. Each cell within the simulation has several counters that count the number of implanted ions, as well as the number of defects (interstitials, vacancies, displacements …) created in the cell. Figure 12.4d shows the result of an actual simulation: a grid of 40×40 cells was used for a nanowire with diameter

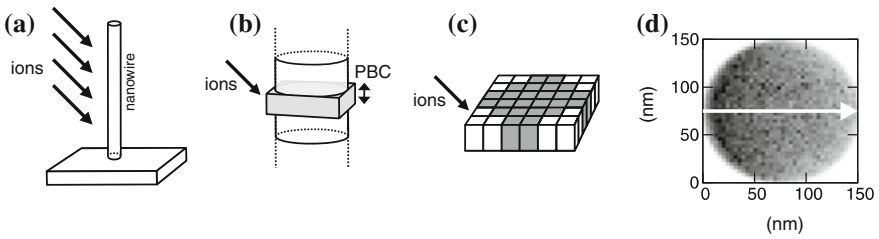

Fig. 12.4 **a** Perpendicular nanowire (NW) irradiated from the side. **b** A segment from a long NW. The *grey shaded box* shows the simulation volume. Periodic boundary conditions (PBC) mimick an infinitely long NW. **c** Simulation volume devided into rectangular cells. **d** Simulation result: each pixel corresponds to one cell (40 × 40). The concentration of implanted ions is shown in greyscale (arbitrary units)

$d = 150$ nm, and each pixel in Fig. 12.4d shows the concentration of implanted ions within one cell in greyscale (arbitrary units).

Results from these simulations with the correct 3D nanowire geometry can be compared to bulk simulations from conventional MC codes. Ion beam implantation is frequently used to dope semiconductors. In order to achieve a quasi-homogeneous doping profile, ions are usually implanted with multiple energies. The homogeneous doping profile is achieved by superposition of the implantation profiles corresponding to the individual ion energies as illustrated in Fig. 12.5a. The implantation profiles were obtained from computer simulations with a conventional MC code with flat surface. Now we use *iradina* to simulate what will happen, if the exact same ion energies and fluencies are implanted into a GaAs nanowire instead of bulk material. The result is shown in Fig. 12.5b: obviously, the concentration of

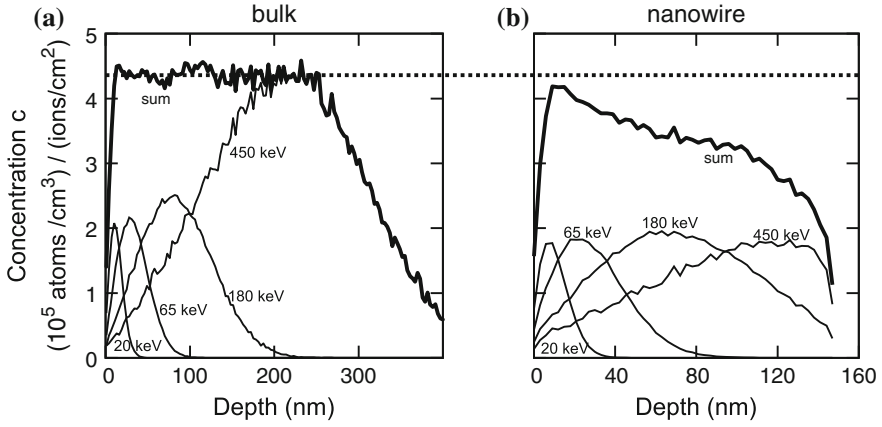

Fig. 12.5 **a** Implantation profile simulated for a bulk target (Zn implantation into GaAs). The profiles for different ion energies (*thin lines*) are superimposed to create a quasi-homogeneous sum profile (*bold line*). **b** The same profile as in (**a**), but simulated for the implantation into a nanowire. The profile corresponds to the *white arrow* in Fig. 12.4d

implanted ions is significantly less in the nanowire than in bulk. For the smallest energy of 20 keV, the profiles differ only marginally, because the ion range is much smaller than the nanowire diameter. For the higher ion energies, the ions are able to exit the nanowire at the side and the back, thus the implantation profiles differ significantly from bulk. Similar differences between bulk and nanowire occur also for the distribution of the irradiation damage. This example clearly shows the necessity to include the correct nanostructure geometry during the Monte Carlo simulation.

It is very interesting to simulate the dynamic changes in shape and structure of the target during ion irradiation. MD codes can inherently do this correctly, but MC codes often assume a static target. However, there have been dynamic MC codes for flat and layered targets for a long time, for example TRIDYN [3]. The codes update the composition of the layers according to implanted ions and ion beam induced damage, and they relax changes in the density by adjusting the layer thicknesses. In three dimensions, these relaxing processes are much more difficult to calculate, but codes for special applications have been reported [16]. More versatile dynamic 3D Monte Carlo simulation codes have only recently been developed (i.e. a 3D version of TRIDYN [17]), some examples being discussed at the end of Sect. 12.5.2. Another interesting approach in this context is the coupling of a FIB topography simulator with a MC code [18].

12.3 Enhanced Dynamic Annealing in Nanostructures

Dynamic annealing is an important effect in damage annihilation during ion irradiation: a fraction of the defects induced by the ion beam can anneal out directly during the irradiation due to the huge amount of energy deposited by the original ion and subsequent ions. Chapter 6 discusses these processes in detail.

The dynamic annealing can be significantly different when nanostructures are irradiated compared to bulk material. The reason lies in the unequal heat dissipation between nanostructures and bulk, as illustrated in Fig. 12.6. The incoming ion loses part of its energy to the target atoms via nuclear energy loss and part via electronic energy loss. Some of the target atoms in the collision cascade are displaced, but

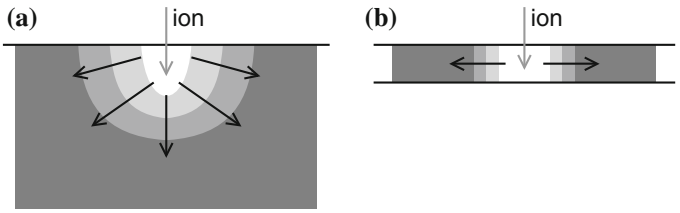

Fig. 12.6 **a** In a bulk target, the heat introduced by the ion can quickly dissipate in all directions. **b** In a nanowire, heat dissipation only proceeds in one dimension

many target atoms receive energy below the displacement threshold. This energy is converted into vibrational energy (phonons) leading to a local heating of the target and consequently possible annealing of defects. Energy transferred to electrons also goes partly into phonons through coupling of the electrons to the lattice, leading to further heating. In bulk material, the heat can quickly dissipate through heat conduction into the complete half-space of the sample. When the dimension of the target is lower, for example a quasi one-dimensional nanowire instead of a 3D bulk target, the heat can only dissipate in one dimension and the dissipation proceeds more slowly. Consequently, there is more time for defects to anneal out than in bulk material; the dynamic annealing is enhanced. A graphic illustration of this phenomenon can be found in [19] where MD simulations of ion impacts on nanowires are presented.

The effect of this enhanced dynamic annealing has been experimentally observed for example by increased amorphization thresholds in Ga ion irradiated GaN nanowires [20]. Such an increase in the amorphization threshold can be visualized directly using transmission electron microscopy (TEM). Figure 12.7a shows a TEM image of a GaAs nanowire, which was initially crystalline and has been implanted at room temperature with manganese ions of 60 keV and a fluence of 2.6×10^{15} cm^{-2} (example taken from [21, 22]). One half of the nanowire was amorphized during irradiation (the side facing the ion beam) but the back side remained crystalline. Computer simulations were performed using *iradina* in order to determine the number and distribution of displacements occuring during the ion implantation; the simulation results are shown in Fig. 12.7b. The number of displacements per lattice atom n_{dpa} obtained from the simulation is compared and overlayed to the TEM image of the nanowire. The amorphization threshold can be determined to be around $n_{\mathrm{dpa}} = 7$, as illustrated in Fig. 12.7c. Due to thinning of the

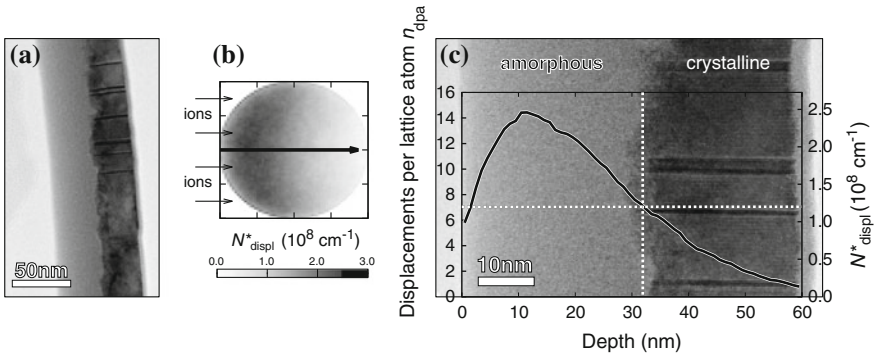

Fig. 12.7 **a** TEM image of a GaAs nanowire (NW) that has been irradiated with Mn ions from the left. Half of the NW was amorphized, the other half remained crystalline. **b** Simulation result from *iradina*: A cross section of the NW is shown, the number of displacement events are coded in greyscale. **c** TEM image of the same NW as in (**a**), but with higher resolution. A plot with the number of displacements obtained from the simulation is overlaid. The profile corresponds to the *thick black arrow* from (**b**)

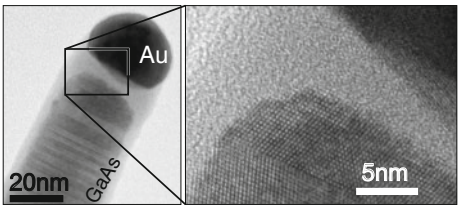

Fig. 12.8 TEM image and high resolution cut out of a GaAs nanowire (NW) that has been irradiated with Mn ions at a temperature of 100 °C and with a fluence of 2×10^{15} cm^{-2}. The dark sphere is the growth seed droplet and consists of gold. The nanowire core remains crystalline except for a thin amorphous neck close to the Au droplet

nanowire through sputtering, the actual amorphization threshold must be corrected to about $n_{\mathrm{dpa}} = 5$. An amorphization threshold of only 2 dpa would be expected from bulk irradiation at room temperature [23]. This example demonstrates the enhancement of dynamic annealing in nanostructures.

The important role of heat conductivity in the dynamic annealing of nanostructures is further shown in the following example: The GaAs nanowire together with its Au tip shown in Fig. 12.8 was irradiated with Mn ions at 100 °C. The heat dissipation is slow in the GaAs material. Consequently, the material remains hot for some time after an ion impact, enabling effective dynamic annealing in the NW core: the core remains crystalline during irradiation. However, an amorphous neck can be observed close to the Au droplet on top. The heat conductivity of the Au is about 6 times higher than of GaAs and the volumetric heat capacity of Au is larger by a factor of ≈1.4 [24]. When ions hit the GaAs close to the Au, the Au acts as an effective heat sink compared to the GaAs, leading to faster cooling and less effective dynamic annealing. Consequently, the neck can be amorphized, while the NW core cannot.

12.4 Semiconductor Nanowires

Semiconductor nanowires have been in the focus of intense research for the past decade, as the quasi one-dimensional structure enables them to serve as both functional unit as well as the wires that access them. Therefore, many different nano-scale applications and proto-type devices based on semiconductor nanowires have already been demonstrated, such as field-effect transistors, sensors, light-emitting diodes, and lasers [25–27]. Beside this huge success, however, full device application in electronics and photonics requires effective and controlled doping, but this is an extremely difficult task during growth of semiconductor nanowires.

In the majority of all cases, the so-called vapor-liquid-solid (VLS) mechanism is used for the growth of semiconductor nanowires, which has already been discovered for the growth of Si whiskers using Au droplets as catalysts in the 1960s [28]. However, in recent years it has been determined that this mechanism cannot fully explain the existing growth of compound semiconductor nanowires [29], because the more volatile component has almost no solubility within the catalyst used. Therefore, diffusion to the interface between catalyst and nanowires as well as

a solid catalyst particle (instead of a liquid one) were introduced in order to explain the stoichiometric semiconductor whisker growth of some III–V compounds [30, 31]. Adding further components such as possible dopants to the growth makes the prediction on the mechanism and the incorporation probability almost impossible. One theoretical work predicted that the dopants preferentially diffuse towards the surface due to low solubility limits and the high surface-to-volume ratio [32]. This effect has been experimentally confirmed for silicon and germanium nanowires below about 20 nm [33]. Another study [34] on germanium nanowires shows a clear inhomogeneous dopant distribution indicating that the vapour-solid (VS) side surface growth is responsible for dopant incorporation rather than the vapour-liquid-solid (VLS) mechanism. Furthermore, it has been observed that doping of silicon nanowires during growth could result in a significant morphological change of the wires [35].

Summarizing, doping of semiconductor nanowires during growth results often in non-uniform doping profiles and dopants accumulate at the sidewalls or surfaces of the semiconductor nanowires; thus, subsequent doping using ion implantation and annealing is a valuable alternative in order to manipulate the electrical, optical or magnetic properties [36, 37].

12.4.1 Ion Beam Doping

Silicon nanowires successfully doped via ion implantation using P and B as dopants in order to realize both n-type and p-type wires, respectively, have first been reported in [38]. The wires used in that study were rather small in diameter and featured an inner crystalline Si core (10–20 nm) and an amorphous SiO_2 shell (5–10 nm). The relatively small size of the wires was chosen with respect to Moore's law, paying regard to the on-going miniaturization in semiconductor technology. In the P implanted wires, partial amorphization took place during the implantation process and recrystallization was obtained after 30 min thermal annealing at 800 °C under high vacuum conditions, as measured by Raman spectroscopy. In the case of B doping, the wires remained crystalline during the whole process. The higher amorphization rate under P irradiation goes with the fact that amorphization is proportional to the ion mass. Fewer defects are created during implantation of the lighter element B and consequently, the enhanced dynamic annealing is sufficient to suppress amorphization. The implanted wires have been prepared as field effect transistors (FETs) for electrical measurements. The geometry with two contact leads (source, drain) to the nanowires on top of a highly doped Si/SiO_2 substrate (gate) is schematically shown in Fig. 12.9a and a typical real device can be seen in the scanning electron microscopy (SEM) image, Fig. 12.9b. The initially ambipolar nanowires show now unipolar I–V characteristics, as it can be clearly seen in the respective transfer curves in Fig. 12.9c, d. This can be connected to an implantation induced band-alignment and successful doping, as the sign of gate voltage (V_G) for the FET ON states is consistent with the implanted impurities. The huge hysteresis

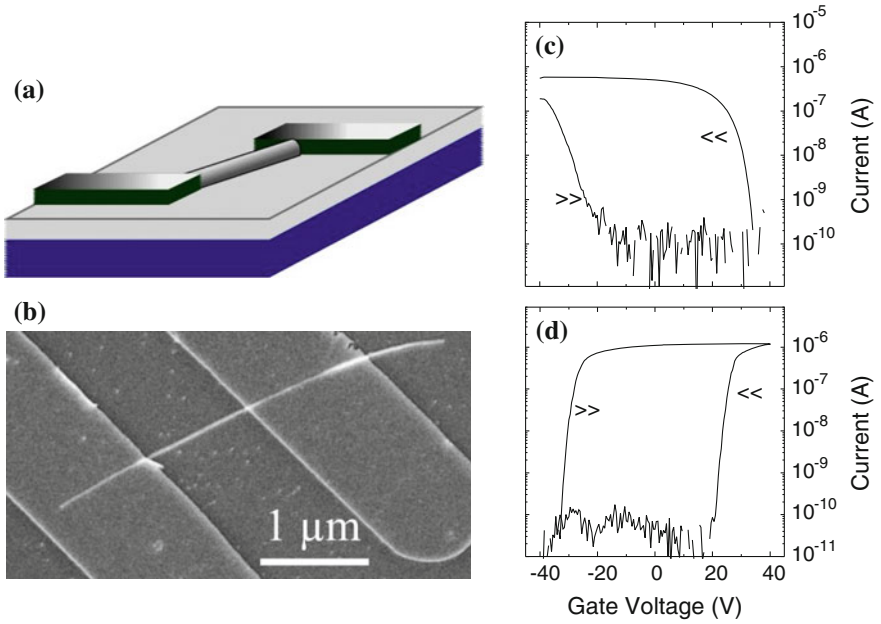

Fig. 12.9 **a** Schematic view of a semiconductor nanowire field effect transistor (FET) contacted with two leads on top of a highly doped Si/SiO_2 substrate. **b** Scanning electron microscope image of a typical FET device with a 1 µm long NW channel. Typical FET transfer curves for **c** P-implanted SiNWs and **d** B-implanted SiNWs. Consecutive gate sweeps for increasing ($\gg$) and decreasing ($\ll$) gate voltage (V_G) are presented. The FET ON state is found for positive V_G in panel (**d**) and for negative V_G in panel (**c**), consistently with the implanted impurities (Data taken from [38])

in the transfer curves is caused by charge traps in the oxide [38], and could be utilized for memory devices.

Ion beam doping of vertically aligned silicon nanowires has been realized [39, 40], as such upstanding nanowires have gained interest as possible building blocks of future 3-dimensional circuits. It has been further demonstrated that even pn-junctions can be realized in vertically aligned nanowires using ion beam doping [39]. Here, relatively thick (diameter 150–400 nm) and up to 500 nm long nanowires have been grown, and ion beam doping was subsequently performed with P as donor and B as acceptor. The ion energies and fluences were carefully chosen in order to realize the situation shown in Fig. 12.10a: boron ions have been implanted with higher energies to form a buried p-type layer. In a second implantation step, low energy phosphorous ions have been used to form the n-type top layer. The nanowires were contacted by a conductive PtIr tip mounted on a nanomanipulator setup inside a SEM, as shown in Fig. 12.10b. Current-voltage measurements clearly showed the rectifying behaviour of the junctions. To verify that the rectifying behaviour originates from the nanowire, electron beam induced current (EBIC) measurements have also been carried out [38]. EBIC can be used for visualization of pn-junctions, and the corresponding mapping

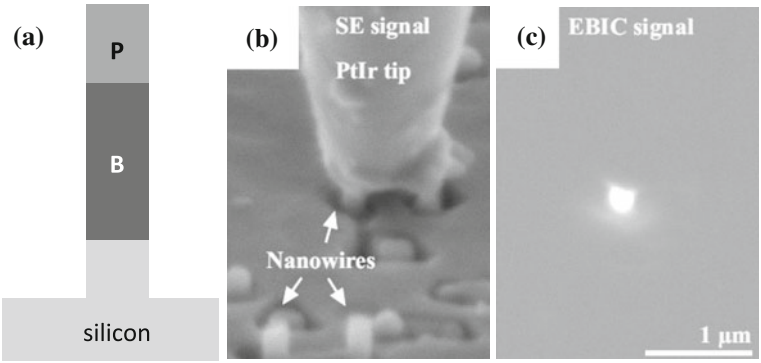

Fig. 12.10 **a** Schematic view of a silicon nanowire with an n-type (phosphorous) on top and a buried p-type (boron) region. **b**, **c** SEM and EBIC images of a nanowire implanted with a profile like shown in (**a**). The nanowires are standing at an angle of 60° with respect to the electron beam (Data taken from [39])

shown in Fig. 12.10c clearly proves that a pn-junction is inside the single silicon nanowire.

Although the optical properties of undoped semiconductor nanowires are already fascinating, doping of those nanostructures with optically active impurities can further enhance the photonic applications. The most interesting impurities are either transition metals (TM) or rare earth (RE) elements as they usually act as luminescence centres in various materials. Various attempts on doping ZnO nanowires with rare earth elements (RE = Ce, Er) during growth were reported not to be successful [41, 42] due to the high melting points of rare earth elements and their composites. Therefore, ZnO nanowires with diameters of 40–60 nm and lengths up to 10 µm were implanted with Yb, Eu, or Tm ions [43]. The majority of the implantation related damage was recovered by thermal annealing at 700 °C for 30 min in O_2 flow [44]. Figure 12.11a shows the photoluminescence of Yb-doped ZnO nanowires in the spectral range of the Yb intra-4f-luminescence. A sharp and intense luminescence peak at 1.260 eV is detected, which can be assigned to the only possible Yb^{3+} transition: $^2F_{5/2} \rightarrow {}^2F_{7/2}$ [45]. A successful activation of the implanted RE elements was also achieved for Eu and Tm in ZnO nanowires, as shown in the cathodoluminescence spectra in Fig. 12.11b, c, respectively. In the case of Eu, the multiple observed transitions can be assigned from the $^5D_0$ level to several ^7F_J $J = 0, \ldots, 6$ levels [46]; whereas, for the Tm case, the emissions are due to $^3H_4 \rightarrow {}^3H_6$ transitions [47] and the splitting is given by different Stark levels as well as contributions from different crystal fields.

Ferromagnetic ordering can be observed in highly Mn-doped GaAs, where Mn provides the uncompensated spins as well as p-doping, allowing hole-mediated ferromagnetism [48]. These diluted magnetic semiconductors (DMS) enable electrically controllable ferromagnetism or spin-FETs for example. Whereas these DMS systems have already been realized in bulk or as thin films, all attempts in the

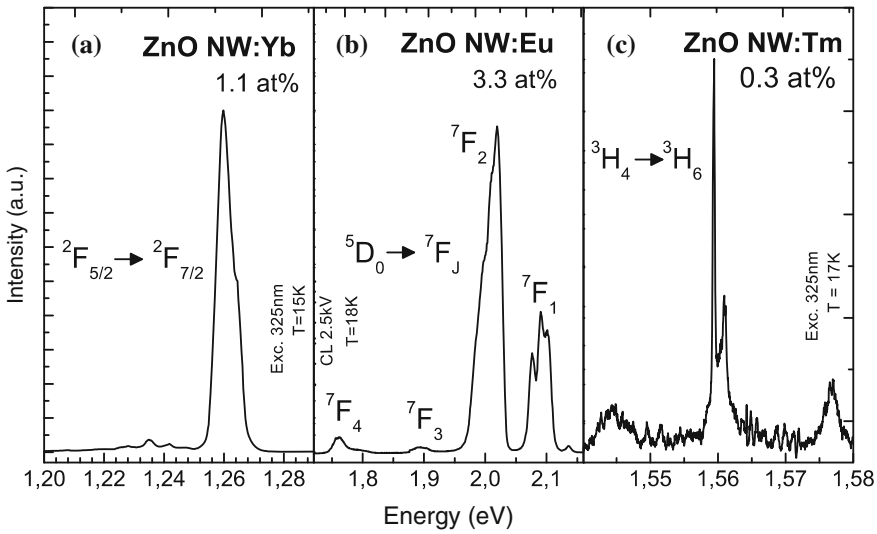

Fig. 12.11 **a** PL spectra of Yb-doped ZnO nanowires: The sharp intra-4f-luminescence of the Yb^{3+} ions originates from the $^2F_{5/2} \rightarrow {}^2F_{7/2}$ transition at 1.26 eV. **b** Intra-4f-luminescence of Eu^{3+} shows a multiplett of transitions from the $^5D_0$ to several ^7F_J levels. **c** Tm-doped ZnO nanowires showing the $^3H_4 \rightarrow {}^3H_6$ transition (Data taken from [43])

growth of highly Mn-doped GaAs nanowires failed, because of the segregation of Mn or MnAs phases during growth leading to non-ideal nanowire morphologies [22]. The only successful realization of high crystalline quality Mn-doped GaAs nanowires reports on the use of ion beam implantation [22], which allows incorporation of dopants into the target material far beyond the solubility limit. In order to minimize ion beam-induced defects different annealing routes were investigated. Post annealing of room temperature implanted and thus amorphous GaAs nanowires (see Fig. 12.7c) was not successful for nanowires, because the nanowires either decomposed or became polycrystalline within the investigated parameter space, as shown in the transmission electron micrograph in Fig. 12.12a. However, heating the sample to higher temperatures during implantation (250 °C) enabled increased dynamic annealing in addition to thermal healing, resulting into single-crystalline $Ga_{1-x}Mn_xAs$ NWs with high Mn content, as demonstrated in Fig. 12.12b. The measured Mn concentration determined by energy dispersive X-ray spectroscopy (EDX) agreed well with corresponding *iradina* simulations [22], and confirmed that respective TRIM simulations overestimate the impurity concentrations, if the nanostructure is in size comparable to the ion range. Magnetotransport measurements on such Mn-implanted and contacted GaAs nanowires (Fig. 12.12d) are displayed in Fig. 12.12c. A strong-temperature dependence of the resistance was observed in addition to a clear negative magentoresistance (MR) at low temperatures. These results indicate dilute Mn

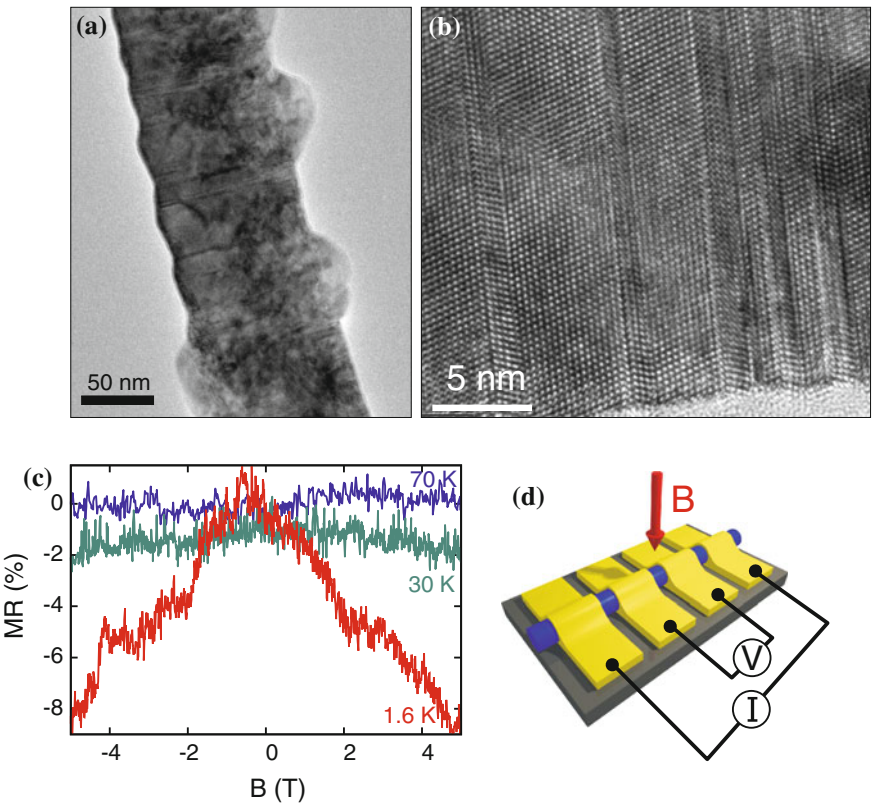

Fig. 12.12 **a** Transition electron micrograph (TEM) of a Mn-implanted GaAs nanowire after annealing in As atmosphere at 550 °C. **b** High resolution TEM micrograph of a GaAs nanowire implanted with x = 5 % Mn at 250 °C without subsequent annealing demonstrating excellent crystalline quality. **c** Plot of magnetoresistance (MR) for different temperatures; a schematic view of the measurement setup is shown in (**d**) (Data taken from [22])

incorporation and, in combination with the observed high resistance of the NWs, support the hypothesis that the implanted NWs are paramagnetic.

12.4.2 Damage Profiles and Bending of Nanowires

Ion beam doping of nanostructures is a useful alternative and tool in order to overcome the limitations of doping during synthesis of nanostructures, as nicely shown above. However, just as for bulk, the ion impact has also a major effect on the structure due to damage creation during irradiation. The effect on nanostructures can even be much more than on bulk [49], if no sufficient compensating dynamic annealing is present. The small size and the free space around nanostructures can

much more easily lead to irreversible structural and mechanical relaxation processes. This results into morphology changes; whereas, in the bulk or thin film situation, the boundary conditions to the surrounding constrain the irradiated volume.

One very interesting issue, which has been investigated in recent years, is how ion beams can shape, bend and even align nanowires [50–53]. While defect creation is mostly considered to be detrimental, the change in shape using ion beams can also be considered as a very helpful tool in controlled manipulation and alignment of nanowires.

Figure 12.13a, b illustrate the damage profiles in nanowires of two extreme situations simulated using *iradina*: the cases of shallow and deep implantation with respect to the nanowire diameter using low and high ion energies, respectively. Here, *iradina* was used in order to calculate vacancies and interstitials in each simulation cell of the nanowire. As one can assume that vacancies and interstitials in vicinity annihilate due to (enhanced) dynamic annealing, the Fig. 12.13a, b show only the value of interstitials minus vacancies for each simulation cell, thus, the number or remaining defects in each cell.

At low ion energies most of the damage is induced on the side of the nanowire that faces the incident ion beam. There is a thin layer with excess vacancies very

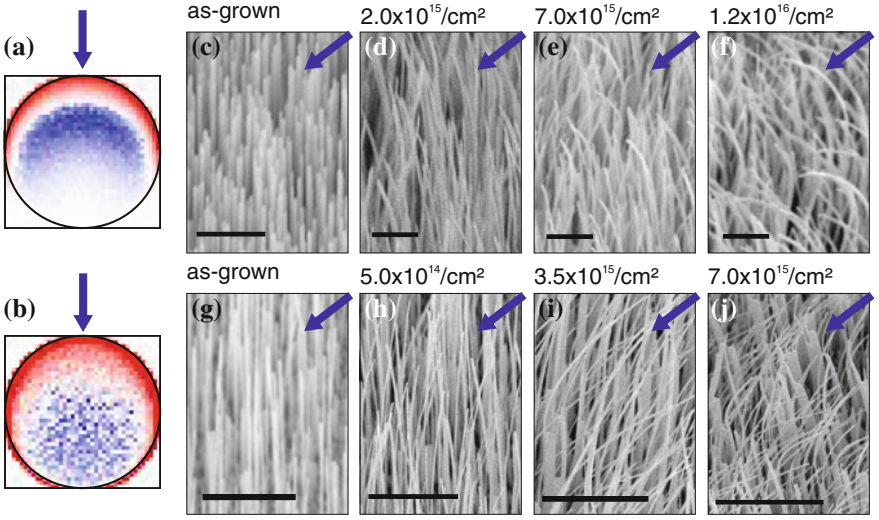

Fig. 12.13 *Iradina* Monte Carlo simulations of ion beam created damage in ZnO nanowires with **a** diameters of 60 nm and 20 keV Ar^+ ions, and **b** diameters of 90 nm and 100 keV Ar^+ ions. *Red* vacancy excess, *blue* interstitial excess. **c–f** SEM images of nanowires (typically 60 nm diameter) irradiated with increasing fluence of 20 keV Ar^+ ions (low energy situation). Scale bars denote 1 μm. **g–j** SEM images of nanowires (typically around 90 nm diameter) irradiated with an increasing fluence of 100 keV Ar^+ ions (high energy situation). Scale bars denote 5 μm. *Arrows* indicate ion beam direction (Data partly taken from [51])

close to the surface of the nanowire, which can be interpreted as removal and sputtering of material. However, most of the upper part of the nanowire is filled with excess interstitials. This additional material leads to a volume expansion of the upper part. Since the lower part is unaffected by the ion beam and not expanded, compressive stress occurs on the irradiated side, while tensile stress is induced on the non-irradiated side. Therefore, a bending moment occurs, which bends the NW away from the ion beam with increasing ion fluence, which can be clearly seen in the experimental findings displayed in the top row of Fig. 12.13.

Opposite, the complete volume of the nanowire is affected by the ion beam for the case of high energy implantation. In this case an excess of vacancies remains in the part facing the ion beam, while excess interstitials remain in the lower part. The vacancies lead to a volume reduction of the upper part of the nanowire, the interstitials to a volume expansion of the lower part. Together, this induces a bending moment, which bends the nanowire towards the incident ion beam. For high fluences, this leads to an alignment of the nanowire axis with the ion beam, as shown in the experimental findings of Fig. 12.13 (bottom row).

This very nice example demonstrates that ion beam induced point defects can have a rigorous effect on the morphology of nanostructures. However, the "negative" effects of ion beam irradiation can also be used in a very positive way: controlled tailoring of the morphology, e.g. for alignment of nanowires!

12.5 Sputtering of Nanostructures

The simulations displayed in Fig. 12.13a, b already show that a high fraction of surface atoms are sputtered, if nanowires are irradiated with ion energies in the keV range. This is obvious, as the ion range is adjusted to the small diameter of the nanowires resulting into the fact that nuclear stopping, which is mainly responsible for sputtering, is the dominating ion-solid interaction process (see above). Now, the interesting question arises, whether sputtering is enhanced for nanostructures compared to perpendicular ion impact on flat surfaces? One can clearly answer this question with "yes", even using just a simple hand-waving argument: a significant fraction of ions hit the surface under an oblique angle and not perpendicular due to the 3D-curvature of nanostructures; and the sputter yield increases with decreasing impact angle [1]. Detailed calculations and simulations corroborate this clear statement [21, 49], but let us first present some experimental observations based on semiconductor nanowires.

Figure 12.14 shows SEM images of ZnO nanowires lying on a Si substrate, which were irradiated with low energy rare earth elements [43]. It is obvious that the morphology of the nanowires dramatically changes with increasing ion fluence. Already after an ion irradiation in the order of 10^{14}–10^{15} cm^{-2} local dimples are visible; whereas, the overall morphology still seems to be flat and unchanged. However, with increasing ion fluence the surface of the nanowires becomes more and more rough, the dimples are deeper, the nanowires become thinner, the cross

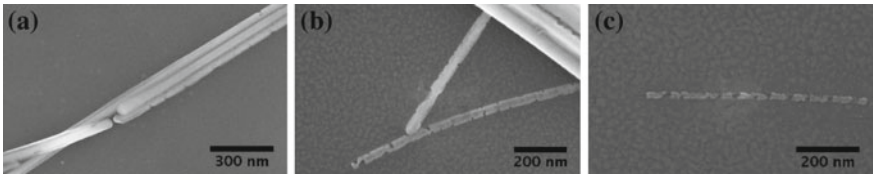

Fig. 12.14 Scanning electron microscopy (SEM) images of ZnO nanowires implanted at room temperature with low energy Eu ions and varying ion fluences: **a** 5.2×10^{14} cm^{-2}, **b** 1.7×10^{15} cm^{-2}, and **c** 5.2×10^{15} cm^{-2} (Data taken from [43])

sections are not round anymore, re-deposited material can be found on the substrate, and finally the nanowires are even cut or completely sputtered away [43, 54]. Such observations do not depend on the ion species used, and are also generally observed during focused ion beam (FIB) milling and for spherical nanoparticles [55]. In the past years, several quantitative studies on the sputter yield of nanostructures under low energy ion irradiation have been presented. It started with theoretical work and simulations, but recently experimental results became available as well. Both will be discussed below.

12.5.1 Static Sputtering Calculations

Semi-analytical models [56] can be used, as well as molecular dynamics (MD) simulations for calculating the size-dependence of the sputter yields of nanoparticles [4] or nanowires [49]. The latter shows that the yield can be up to threefold compared to bulk due to the enhanced formation of defects on or near the surface, because their formation energy is lower than in bulk. *Iradina* can also be used to simulate ion beam irradiation of nanoparticles and obtain the sputter yield as a function of nanoparticle size. In order to compare results from *iradina* to the MD method and to experimental data, we show one example: irradiation of Au nanoparticles with Ga^+ ions at energies from 0 to 30 keV (typical conditions in a focussed ion beam system).

Figure 12.15 shows the calculated sputter yield of spherical Au nanoparticles, (a) irradiated with 25 keV Ga^+ ions as a function of nanoparticle diameter, and (b) for a constant diameter as a function of ion energy. Very small NPs have a low sputter yield, which can be explained by the fact that the ions only deposit a small fraction of their energy within the nanoparticles before they leave the nanoparticle again. The sputter yield quickly increases with diameter d and reaches a maximum at about $d =$ 8–10 nm. This size is approximately the same as the projected range of the ions in bulk material (8.3 nm): the ions deposit most of their energy within the particle, but the particle is still so small, that a large fraction of the kinematic energy in the collision cascades reaches the surface of the particle. At larger diameters, the sputter yield decreases again. The reason is that now the collision cascades will

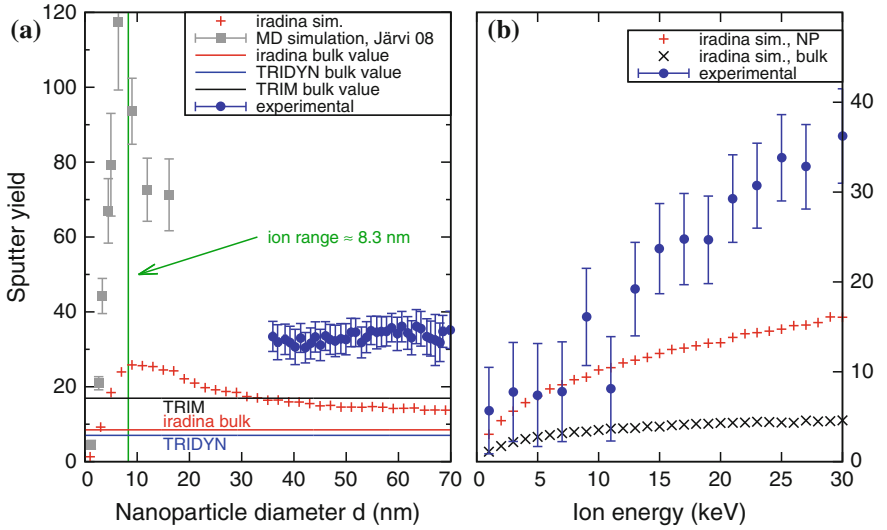

Fig. 12.15 **a** Size dependence of sputter yield for irradiation of Au NPs with 25 keV Ga^+ ions (surface binding energy $E_S = 3.8$ eV) calculated by *iradina* and measured experimentally. MD simulation results from [4] are shown for comparison. The bulk sputter yields for perpendicular incidence are illustrated as calculated by TRIM [1], TRIDYN [3] and *iradina*. **b** Energy dependence of the sputter yield for irradiation of Au NPs (diameter 50 nm) with Ga^+ ions: simulations and experimental results. Simulated sputtering for bulk material is shown for comparison (Experimental and simulated data taken from [57])

often not extend to the surface or the kinematic energy in the collision cascades is to a large extend absorbed within the particle and does not reach the surface. For very large nanoparticles with $d > 150$ nm, the sputter yield converges (not shown in the figure). Here, the nanoparticles are much larger than the projected range, thus they appear to the ions as bulk. However, the sputter yield does not reach the bulk value, which was calculated for perpendicular incidence and is similar for *iradina* and TRIDYN. The reason is simply that the incidence angles of the ions hitting the particle at different locations are always distributed between 0° and 90°, no matter how large the nanoparticle becomes and the sputter yield depends strongly on this angle of incidence, as already argued above in the hand-waving discussion.

The general behaviour and trend of the sputter yield obtained from *iradina* is similar to the MD results [4], as illustrated in Fig. 12.15a. This clearly underlines our previous hand-waiving argument that the sputter yield for nanostructures is enhanced and strongly depends on the size and shape of the nanostructures. The difference between the MC and MD simulations are the absolute sputter yields. However, one cannot expect MC and MD simulations to yield the same results. For instance, the MD simulations will be more accurate for very small nanoparticles: while Monte Carlo (MC) simulations intrinsically assume a static solid with a temperature of 0 K, the MD allows all atoms to be in motion and can represent temperatures >0 K. In the MD, heating of the nanoparticle by the ion impact and

subsequent thermal (non-ballistic) evaporation of Au atoms is possible—as opposed to MC simulations. The following estimation shows the importance of this effect: consider a small Au nanoparticle of 10 000 atoms (≈7 nm diameter). Even if an ion deposits only 1 keV into heat, this accounts for an average of 100 meV per atom, corresponding to a temperature of about 900 °C, which can lead to thermal evaporation of atoms. Furthermore, the MD can simulate emission of small Au clusters with several atoms, which requires less energy than to sputter each atom individually. The MD shows [4] indeed that about 30 % of sputtered Au is emitted in clusters of two or more Au atoms. More recent MD simulations corroborate the fact, that sputtering of nanosized objects can strongly be increased and dominated by cluster emission [5]. Nevertheless, the MD simulations allow only limited target sizes and small ion numbers due to the extremely large computation times required.

Sputter yields of Au nanoparticles irradiated with Ga ions where also investigated experimentally [57]. As shown in Fig. 12.15a, the experimental sputter yields run in parallel with the simulation results by *iradina*, but are shifted to higher values. Unfortunately, there are up to now no experimental data on smaller nano particles with diameters around 10 nm at the expected maximum in the sputter yield. There are different reasons for experimental sputter yields being higher compared to the MC simulations: as explained above, thermal effects and cluster emission, both not taken into account in the MC simulation, increase the sputter yield. Furthermore, the experiments were performed with NPs deposited on a silicon substrate while the simulations were done with free NPs neglecting NP-substrate interaction. When NPs are attachted to a substrate, on the one hand the sputter yield of the NP itself is decreased because sputtering in forward direction is suppressed, but on the other hand, the yield is increased by ions hitting the substrate close to the NP, because their damage cascades and thermal deposition of energy can reach into the NP. The experimental sputter yield as a function of ion energy, shown in Fig. 12.15b shows the same trend as the simulations but has a steeper slope for the same reasons as described above. MD simulations might fit the experimental data in the future, when sufficient computational resources become available to simulate larger nanoparticles.

12.5.2 Dynamic Sputtering Calculations

For high fluence irradiation, the assumption of a static target in Monte Carlo simulations becomes increasingly inaccurate, for different reasons: For example, when a nanowire is doped with high doses by ion beam implantation, it becomes thinner due to sputtering, which changes the implantation profiles. Furthermore, a significant change in composition due to the incorporated atoms may change the sputter yield. Another important effect is redeposition of sputtered atoms when a nanostructure is placed on a substrate, or when many nanoparticles are close to each other. In order to take all such effects into account in a simulation, the target structure and composition must be allowed to change *dynamically* during the

simulation. While MD simulations intrinsically include a dynamic target, they can (yet) only cover small target structures and small ion numbers. Dynamic Monte Carlo binary collision simulations have been possible since many years using the TRIDYN code [3]. Recently, this code was extended to fully three-dimensional targets "TRI3DYN" [17] and thus allows to simulate high fluence ion beam irradiation effects in nanostructures.

For example, high dose ion beam doping by axial implantation into nanowires has recently been studied using TRI3DYN [58]. The dynamic simulations show that the resputtering of implanted dopant atoms plays a very important role in nanostructures and quickly limits the achievable final doping concentration—an effect not accessible by static simulations. Such effects will become more important in the future, as 3D-nanostructured substrates are gaining importance in new semiconductor device concepts.

The sputtering of ZnO nanowires under Mn ion beam implantation and the incorporation of Mn dopant atoms has also been studied by pseudo-dynamic simulations using *iradina* [59]. Here, "pseudo-dynamic" means that the simulation code features a static target only, however, a number of static simulations is made incrementally to mimic a dynamic simulation: a small fluence step can be simulated with a static target, the output of the simulation can be used to construct a revised target geometry, which is then used as input for the next step in the simulation. When considering a limited set of target geometries, an alternative is to make a set of simulations for all possible geometries first and subsequently calculate a dynamic process incrementally by selecting the appropriate simulation results.

The latter approach is shown in Fig. 12.16 for ZnO nanowires implanted with manganese (and rotated during implantation) as blue squares. Sputter yields and doping efficacy were precalculated for different NW diameters and Mn/Zn ratios. The dynamic behaviour of the NW during Mn implantation was calculated step-wise, starting with a NW of 200 nm diameter, and subsequently reducing diameter and increasing Mn/Zn ratio according to the appropriate simulation results. The Mn concentration increases linearly at first and in good agreement with the experimental data (red circles in Fig. 12.16). While the NW diameter decreases due to sputtering, the Mn concentration increases slightly super-linearly in the range between 1 and 2×10^{17} cm^{-2}. With further increasing fluence and decreasing diameter, a larger fraction of the Mn ions passes through the nanowire and is not implanted anymore, leading to a saturation of the achieved Mn concentration, which can clearly be seen in Fig. 12.16. At high fluencies, the experimental data of the Mn/Zn ratio begin to deviate from the calculated values, because the simulation inaccurately presumes a homogeneous doping profile [60, 61]. However, in reality the core of the NW is enriched in Mn, because when Mn atoms come near to the surface during implantation, they have a high probability to leave the nanowire and not become implanted. Consequently, less Mn is sputtered away later and furthermore, when the nanowire is thinned, the Mn-rich core is what is left over.

In order to avoid the problems of the pseudo-dynamic simulation, a full dynamic simulation of the implantation experiment can be made. For this purpose, a special

version of *iradina* was adapted to allow a dynamic composition variation of a cylindrical nanowire. The geometry in this version is defined by nested cylinders of flexible radius instead of the static rectangular cells as described in Sect. 12.2. Since the nanowire is rotated around its axis during irradiation, full rotational symmetry is maintained at all times. Furthermore, a long nanowire can mostly be considered to be invariant under translation along its axis. Thus, the radius is the only free dimension, and the concentration profile within the nanowire can be described by a one-dimensional function. The dynamic concentration profile is then calculated in a manner similar to TRIDYN [3]: when the simulation produces interstitials and vacancies, the effective density within each cylinder changes. The radii of all cylinders are then adapted in such a way as to relax the densities to their nominal values. Note, however, that only the dynamic composition variation is one-dimensional, the ion transport simulation itself is still fully three-dimensional.

The results of this dynamic simulation are illustrated in Fig. 12.16 as a green line. For small fluencies, the resulting Mn/Zn-ratio is close to the pseudo-dynamic results. With increasing fluence, the dynamic simulation matches the trend of the experimental data more closely than the pseudo-dynamic simulation, because the dynamic simulation takes into account the inhomogeneous Mn doping profile. At very high fluencies or very small diameters, respectively, the Mn/Zn-ratio curve becomes rather unsmooth. In this case, only few material is left in the nanowire, and single ion events can have a large influence on the concentration.

This example illustrates the importance of dynamic calculations for the case of high fluence implantation in nanostructures.

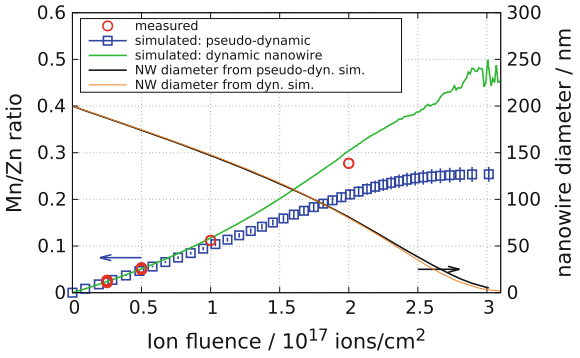

Fig. 12.16 Doping of a ZnO nanowire by 180 keV Mn ion implantation (with the NW rotated about its axis during implantation). The Mn/Zn ratio is shown as a function of ion fluence, calculated by pseudo-dynamic and by dynamic simulations using *iradina* and compared to experimental data. The *right* axis shows to calculated diameter of the nanowire to illustrate thinning by sputtering. Experimental data and pseudo-dynamic simulation results are taken from [59]

12.6 Summary

This chapter outlines the important role that ion beams play in the modification of nanostructures. Doping during growth of nanostructures is often very difficult due to thermodynamic constraints. Ion beam implantation with energies far above thermal energies is thus a very useful tool to overcome solubility limits and dope semiconductor nanostructures after growth. For example semiconductor nanowires (NW) have successfully been modified with electrically, optically, or magnetically active dopands using ion beams: NW field effect transistors have been created, pn-junctions in perpendicular NWs have been realized, optical emission from various rare earth atoms in NWs has been observed, and paramagnetic semiconductor nanowires have been created.

However, there are substantial differences when irradiating nanostructures as compared to bulk material or thin film systems, especially for free-standing nanostructures and as soon as the size of the nanostructure is comparable to the mean ion range. First of all, the distribution of the implanted ions in the target differs between nanostructures and bulk. Computer simulations of the ion irradiation of nanostructures must therefore take into account the correct 3D geometry of the target (this is for example possible using *iradina*). Furthermore, nanostructures have a large surface-to-volume ratio. This leads to strongly enhanced sputter yields reaching a maximum when the ion range is comparable to the size of the nanostructure. This increased sputtering is oberserved experimentally for nanowires and can be calculated by different methods for spherical nanoparticles. A further important difference lies in the dynamic annealing, which is enhanced in nano-structures. The reason is the slower dissipation of heat due to the confined dimensions. These differences must be taken into account when planning ion implantation experiments with nanostructured targets. In particular, the optimum implantation temperatures and annealing procedures cannot simply be adopted from bulk experiments but must be appropriately adjusted.

Special care has to be taken for high fluence irradiation of nanostructures, for example for alloying. Here, dynamic calculations are mandatory as enhanced sputtering and resputtering of implanted atoms can lead to a non-linear behaviour of dopant concentration as a function of dose and to significant changes in the target geometry.

Finally, ion beam irradiation can invoke new effects in free-standing nanostructures, which are not known from bulk irradiation. An example is the ion beam induced bending of nanowires, which is caused by an unequal distribution of ion beam induced point defects. This effect can even be used to align nanowires to a desired direction. It represents a neat example how low energy ion irradiation can be utilized to tailor the structure and morphology of nanostructures beyond “just” doping.

Acknowledgements We thank Dr. Raphael Niepelt and Dr. Sebastian Geburt for planning, performing and evaluating many of the nanowire implantation experiments presented here. Furthermore, we thank Prof. Dr. Wolfhard Möller for valuable discussion about the simulation

codes and Dr.Maria Messing for recording some of the TEM images. We acknowledge financial support for the nanowire implantation experiments by the DFG under grants Ro1198/7-3 and FOR1616.

References

1. J.F. Ziegler, J.P. Biersack, U. Littmark, *Stopping and Range of Ions in Solids* (Pergamon, New York, 1985)
2. A. Mutzke, R. Schneider, W. Eckstein, R. Dohmen, SDTrimSP version 5.00. IPP Report 12/8, Max-Planck-Institut für Plasmaphysik, Garching, Germany (2011)
3. W. Möller, W. Eckstein, Nucl. Instr. Meth. B **2**, 814 (1984)
4. T.T. Järvi, J.A. Pakarinen, A. Kuronen, K. Nordlund, Europhys. Lett. **82**, 26002 (2008). doi:10.1209/0295-5075/82/26002
5. G. Greaves, J.A. Hinks, P. Busby, N.J. Mellors, A. Ilinov, A. Kuronen, K. Nordlund, S.E. Donnelly, Phys. Rev. Lett. **111**, 65504 (2013). doi:10.1103/PhysRevLett.111.065504
6. W. Boxleitner, G. Hobler, Nucl. Instr. Meth. B **180**, 125 (2001)
7. H.B. Kim, G. Hobler, A. Steiger, A. Lugstein, E. Bertagnolli, Nanotechnology **18**, 245303 (2007)
8. G. Hobler, S. Selberherr, IEEE Trans. Comput. Aided Des. Integr. Circuits Sys. **8**, 450 (1989). doi:10.1109/43.24873
9. B.J. Obradovic, G. Balamurugan, G. Wang, Y. Chen, A.F. Tasch, in *International Electron Devices Meeting, 1998. IEDM '98 Technical Digest.* (1998), pp. 513–516. doi:10.1109/IEDM.1998.746410
10. H. Stippel, S. Selberherr, in *Proceedings of VPAD* (1993), pp. 122–123. URL http://in4.iue.tuwien.ac.at/pdfs/vpad1993/pdfs/00724750.pdf
11. A. Burenkov, K. Tietzel, A. Hossinger, J. Lorenz, H. Ryssel, S. Selberherr, in *International Conference on Simulation of Semiconductor Processes and Devices* (IEEE, 1999), pp. 55–58, 6–8 September 1999. doi:10.1109/SISPAD.1999.799258
12. B. Yuan, F. Yu, S. Tang, Nucl. Instr. Meth. B **83**, 413 (1993)
13. F. Schiettekatte, Nucl. Instr. Meth. B **266**, 1880 (2008)
14. C. Borschel, C. Ronning, Nucl. Instr. Meth. B **269**, 2133 (2011). doi:10.1016/j.nimb.2011.07.004
15. Iradina, Download page (2013). URL http://www.iradina.de
16. R. Collins, A. Prez-Martn, J. Domnguez-Vzquez, J. Jimnez-Rodrguez, Nucl. Instr. Meth. B **90**, 433 (1994). doi:10.1016/0168-583X(94)95588-3
17. W. Möller, Nucl. Instr. Meth. B **322**, 23 (2014). doi:10.1016/j.nimb.2013.12.027
18. D. Kunder, E. Baer, M. Sekowski, P. Pichler, M. Rommel, Microelectr. Eng. **87**, 1597 (2010)
19. H.M. Urbassek, R.M. Bradley, M.L. Nietiadi, W. Möller, Phys. Rev. B **91**, 165418 (2015). doi:10.1103/PhysRevB.91.165418
20. S. Dhara, A. Datta, C.T. Wu, Z.H. Lan, K.H. Chen, Y.L. Wang, L.C. Chen, C.W. Hsu, H.M. Lin, C.C. Chen, Appl. Phys. Lett. **82**, 451 (2003). doi:10.1063/1.1536250
21. C. Borschel, Ion-solid interaction in semiconductor nanowires, Dissertation, University of Jena, 2012. URL http://www.db-thueringen.de/servlets/DocumentServlet?id=20026
22. C. Borschel, M.E. Messing, M.T. Borgström, W. Paschoal, J. Wallentin, S. Kumar, K. Mergenthaler, K. Deppert, C.M. Canali, H. Pettersson, L. Samuelson, C. Ronning, Nano Lett. **11**, 3935 (2011). doi:10.1021/nl2021653
23. R.A. Brown, J.S. Williams, J. Appl. Phys. **81**, 7681 (1997). doi:10.1063/1.365347
24. Memsnet materials database (2012). URL www.memsnet.org
25. C. Lieber, Z. Wang (eds.), *Functional Nanowires*, vol. 32 (2007)
26. C. Jagadish (ed.), *Special issue on Nanowires*, vol. 25 (2010)
27. C. Ning, Phys. Stat. Sol. B **247**, 774 (2010)

28. R.S. Wagner, W.C. Ellis, Appl. Phys. Lett. **4**, 89 (1964)
29. C. Borchers, S. Müller, D. Stichtenoth, D. Schwen, C. Ronning, J. Phys. Chem. B **110**, 1656 (2006)
30. K.A. Dick, K. Deppert, T. Martensson, B. Mandl, L. Samuelson, W. Seifert, Nano Lett. **5**, 761 (2005)
31. J. Johansson, C.P.T. Svensson, T. Martensson, L. Samuelson, W. Seifert, J. Phys. Chem. B **109**, 13567 (2005)
32. M.V. Fernandez-Serra, C. Adessi, X. Blase, Phys. Rev. Lett. **96**, 166805 (2006)
33. P. Xie, Y. Hu, Y. Fang, J. Huang, C.M. Lieber, Proc. Natl. Acad. Sci. USA **106**, 15254 (2009). doi:10.1073/pnas.0906943106
34. D.E. Perea, E.R. Hemesath, E.J. Schwalbach, J.L. Lensch-Falk, P.W. Voorhees, J.L. Lauhon, Nature Nanotechnol. **4**, 315 (2009). doi:10.1038/nnano.2009.51
35. S.J. Whang, S. Lee, D.Z. Chi, W.F. Yang, B.J. Cho, Y.F. Liew, D.L. Kwong, Nanotechnology **18**, 275302 (2007). doi:10.1088/0957-4484/18/27/275302
36. C. Ronning, C. Borschel, S. Geburt, R. Niepelt, Mat. Sci. Eng. R. R. **70**, 30 (2010). doi:10.1016/j.mser.2010.07.002
37. C. Ronning, C. Borschel, S. Geburt, R. Niepelt, S. Müller, D. Stichtenoth, J.P. Richters, A. Dev, T. Voss, L. Chen, W. Heimbrodt, C. Gutsche, W. Prost, Phys. Stat. Sol. B **247**, 2329 (2010). doi:10.1002/pssb.201046192
38. A. Colli, A. Fasoli, C. Ronning, S. Pisana, S. Piscanec, A.C. Ferrari, Nano Lett. **8**, 2188 (2008)
39. S. Hoffmann, J. Bauer, C. Ronning, T. Stelzner, J. Michler, C. Ballif, V. Sivakov, S.H. Christiansen, Nano Lett. **9**, 1341 (2009). doi:10.1021/nl802977m
40. P.D. Kanungo, R. Kögler, K. Nguyen-Duc, N. Zakharov, P. Werner, U. Gösele, Nanotechnology **20**, 165706 (2009). doi:10.1088/0957-4484/20/16/165706
41. T. Hirate, S. Sasaki, W. Li, H. Miyashita, T. Kimpara, T. Satoh, Thin Solid Films **487**, 35 (2005). doi:10.1016/j.tsf.2005.01.031
42. B. Cheng, Y. Xiao, G. Wu, L. Zhang, Adv. Funct. Mater. **14**, 913 (2004). doi:10.1002/adfm.200305097
43. S. Geburt, D. Stichtenoth, S. Müller, W. Dewald, C. Ronning, J. Wang, Y. Jiao, Y.Y. Rao, S. K. Hark, Q. Li, J. Nanosci. Nanotechnol. **8**, 244 (2008). doi:10.1166/jnn.2008.N05
44. C. Ronning, P.X. Gao, Y. Ding, Z.L. Wang, D. Schwen, Appl. Phys. Lett. **84**, 783 (2004). doi:10.1063/1.1645319
45. G. Dieke, *Spectra and Energy levels of Rare Earth Ions in Crystals* (Interscience Publishers, New York, 1968)
46. C. Cascales, M.D. Serrano, F. Esteban-Betegón, C. Zaldo, R. Peters, K. Petermann, G. Huber, L. Ackermann, D. Rytz, C. Dupré, M. Rico, J. Liu, U. Griebner, V. Petrov, Phys. Rev. B **74**, 174114 (2006). doi:10.1103/PhysRevB.74.174114
47. S. Bachir, J. Ronfard-Haret, K. Azuma, D. Kouyat, J. Kossanyi, Chem. Phys. Lett. **213**, 54 (1993). doi:10.1016/0009-2614(93)85417-M
48. H. Ohno, A. Shen, F. Matsukura, A. Oiwa, A. Endo, S. Katsumoto, Y. Iye, Appl. Phys. Lett. **69**, 363 (1996). doi:10.1063/1.118061
49. W. Ren, A. Kuronen, K. Nordlund, Phys. Rev. B **86**, 104114 (2012). doi:10.1103/PhysRevB.86.104114
50. C. Borschel, R. Niepelt, S. Geburt, C. Gutsche, I. Regolin, W. Prost, F.J. Tegude, D. Stichtenoth, D. Schwen, C. Ronning, Small **5**, 2576 (2009). doi:10.1002/smll.200900562
51. C. Borschel, S. Spindler, D. Lerose, A. Bochmann, S.H. Christiansen, S. Nietzsche, M. Oertel, C. Ronning, Nanotechnology **22**, 185307 (2011). doi:10.1088/0957-4484/22/18/185307
52. L. Romano, N.G. Rudawski, M.R. Holzworth, K.S. Jones, S.G. Choi, S.T. Picraux, J. Appl. Phys. **106**, 114316 (2009). doi:10.1063/1.3267154
53. K. Jun, J. Joo, J.M. Jacobson, J. Vac. Sci. Tech. B **27**, 3043 (2009). doi:10.1116/1.3259919
54. D. Stichtenoth, Dimensionseffekte in Halbleiternanodrähten, Dissertation, University of Göttingen, 2008. URL http://webdoc.sub.gwdg.de/diss/2008/stichtenoth/
55. O. Dmitrieva, B. Rellinghaus, J. Kästner, M.O. Liedke, J. Fassbender, J. Appl. Phys. **97**, 10N112 (2005). doi:10.1063/1.1853211

56. A. Klimmer, P. Ziemann, J. Biskupek, U. Kaiser, M. Flesch, Phys. Rev. B **79**, 155427 (2009). doi:10.1103/PhysRevB.79.155427
57. H. Holland-Moritz, S. Scheeler, C. Stanglmair, C. Pacholski, C. Ronning, Nanotechnology **26**, 325301 (2015). doi:10.1088/0957-4484/26/32/325301
58. W. Möller, K.H. Heinig, Collisional transport in ion-irradiated nanowires. Personal communication (2015)
59. A. Johannes, High-fluence ion beam irradiation of semiconductor nanowires, Dissertation, University of Jena, 2015
60. A. Johannes, S. Noack, W. Paschoal, S. Kumar, D . Jacobsson, H. Pettersson, L. Samuelson, K.A. Dick, G. Martinez-Criado, M. Burghammer, C. Ronning, J. Phys. D Appl. Phys. **47**, 394003 (2014). doi:10.1088/0022-3727/47/39/394003
61. A. Johannes, S. Noack, W. Paschoal, S. Kumar, D. Jacobsson, H. Pettersson, L. Samuelson, K. A. Dick, G. Martinez-Criado, M. Burghammer, C. Ronning, J. Phys. D Appl. Phys. **48**, 079501 (2015). doi:10.1088/0022-3727/48/7/079501